UDC 524.3-52
RSTI 41.25.29

https://doi.org/10.55452/1998-6688-2026-23-1-334-345

[1]Abdirakhman A.,
Master's student, ORCID ID: 0009-0002-0532-9641,
e-mail: armiyaqyzyaidana@gmail.com
[1,2]Omar A.,
PhD, ORCID ID: 0000-0002-5604-3742,
*e-mail: omaruzhan@gmail.com
[1]Islyam Zh.,
Master's student, ORCID ID: 0009-0006-5496-4501,
e-mail:islyamovzhomart@gmail.com
[1,2]Alimgazinova N.,
Cand. Phys.-Math Sc., ORCID ID: 0000-0002-4596-1855,
e-mail: Nazgul.Alimgazinova@kaznu.kz
[1,2]Demessinova A.,
PhD, ORCID ID: 0000-0001-5049-9338,
e-mail:aizat.dem@gmail.com
[1]Nodyarov A.,
PhD, ORCID ID: 0000-0002-0045-5457,
e-mail: nodyarov.atilkhan@gmail.com
[3]Tuiakbaeva D.,
Master's student, ORCID ID: 0009-0003-8572-1850,
e-mail: duria1510@outlook.com
[2,4]Manapbayeva A.,
PhD, ORCID ID: 0000-0002-0322-1509
e-mail: manapbayeva.arailym@gmail.com
[1]Adilzhan K.,
PhD student, ORCID ID: 0000-0003-4136-3935,
e-mail: kami_adilzhan@mail.ru
[5]Shaimoldin N.,
PhD student, ORCID ID: 0000-0001-9557-8590,
e-mail: nurzhan@xao.ac.cn

[1]Al-Farabi Kazakh National University, Almaty, Kazakhstan
[2]Institute of Experimental and Theoretical Physics,
Al-Farabi Kazakh National University, Almaty, Kazakhstan
[3]Sh. Ualikhanov Kokshetau University, Kokshetau, Kazakhstan
[4]Kazakh National Women's Teacher Training University, Almaty, Kazakhstan
[5]Xinjiang Astronomical Observatory, Chinese Academy of Sciences, Urumqi, China

KINEMATICS AND STRUCTURE OF THE MASSIVE STAR-FORMING REGION G350.29+0.12

Abstract

We present high–angular resolution 1.3 mm continuum and molecular line observations toward the high-mass star-forming region G350.29+0.12, using CH_3CN and $CH_3{}^{13}CN$ rotational transitions. The continuum emission resolves two main cores: a bright, compact northern core G350.29+0.12 A and a weaker southern core G350.29+0.12 B. Core A exhibits six compact substructures embedded within more extended emission. Multiple

K-components of the CH_3CN J = 14→13 and $CH_3{}^{13}CN$ J = 14→13 transitions are detected, with the emission arising primarily from core A. The CH_3CN moment 0 maps show that the integrated intensities peak at the main continuum position, indicating that the molecular emission traces warm and dense gas. The moment 1 maps reveal a pronounced velocity gradient of ∼2 km s^{-1} across core A, oriented from northwest to southeast, while the moment 2 maps show K-dependent variations in velocity dispersion. Position–velocity diagrams further indicate organized rotational motions, exhibiting a compact velocity structure with a central peak and systematic gradients. Rotational temperature analysis yields = 360.6 ± 34.8 K for CH_3CN, tracing the hottest and densest gas and T_{rot} = 138 ± 45 K for $CH_3{}^{13}CN$, consistent with cooler and more extended material. Together, these results demonstrate that G350.29+0.12 A is a rotating hot molecular core undergoing active high-mass star formation.

Keywords: massive star-forming region, molecular emission, position–velocity analysis, rotational temperature, hot molecular core.

Received: January 21, 2026; accepted: March 10, 2026.

Introduction

Massive stars (with masses greater than 8 solar masses, $M > 8\ M_{\odot}$) originate within large, dense molecular clumps, typically spanning around 1 pc with densities of $10^4 – 10^5$ cm^{-3} and masses of approximately $10^3 M_{\odot}$. These environments are characterized by significant turbulent motions that strongly influence and support their gas structures [1, 2]. High-mass star-forming regions (HMSFRs) represent the earliest and most dynamic phases of massive star birth within the interstellar medium, exhibiting intricate chemical complexity. Kinematic studies are crucial for understanding the physical processes at play, as signatures of infall, rotation, and large-scale accretion flows serve as key indicators of gravitational collapse and stellar mass buildup [3, 4].

Massive star formation often occurs within highly dynamic molecular complexes shaped by large-scale processes like cloud-cloud collisions and filamentary accretion, which compress gas and promote clustered star formation [5–7]. These mechanisms can significantly enhance star formation efficiency and even drive core-core interactions within dense clumps, accelerating the growth of massive protostars [8]. Alternatively, similar morphologies can result from hub-filament systems, where gravitationally focused flows channel material from extended filaments into central dense cores [9, 10]. Many HMSFRs indeed display hub-filament networks with converging flows continuously feeding the central structures [11, 12]. Furthermore, stellar feedback from evolved sources can either trigger or suppress subsequent star formation, depending on local physical conditions [13].

Understanding the physical dynamics and chemical complexity within star-forming environments relies heavily on the use of molecular tracers. Studies aimed at determining the density structure, kinematics, and chemical composition of dense gas emphasize the role of gas distribution [14–16], shock-driven processes [17], and departures from chemical equilibrium [18]. Together, these observations provide a fundamental basis for interpreting the evolution of massive stars and their surrounding environments. Insights into dynamic and chemically rich star-forming environments can be informed by approaches developed for other rapidly evolving astrophysical systems, where early multi-wavelength observations have proven essential for characterizing their physical and chemical properties [19].

Complex organic molecules (COMs), defined as carbon-bearing species with six or more atoms, are particularly relevant in this context. Their formation involves both gas-phase reactions and grain-surface chemistry, which are active areas of research. Symmetric top molecules, such as methyl cyanide (CH_3CN) and its isotopologues (e.g., $CH_3{}^{13}CN$), are excellent tracers of gas temperature and excitation conditions, making them key diagnostics for studying the physical and chemical evolution of HMSFRs [20]. In this study, we present high-angular-resolution ALMA Band 6 observations of G350.29+0.12, focusing on highly excited transitions of CH_3CN and $CH_3{}^{13}CN$.

Materials and methods

We analyzed archival ALMA Band 6 data (Project 2018.1.00794.S) obtained on 2018 December 5 to investigate the molecular line emission toward the G350.29+0.12 region, which has a systemic velocity of −63 km s^{-1}. The dataset covers six spectral windows spanning 240.83–260.637 GHz with a frequency resolution of 282.1974 kHz. The observations were conducted with the ALMA 12-m array configuration, providing baseline lengths between 45.201 and 328.761 m and yielding an angular resolution of 0.415″, with a synthesized beam size of 0.397″ × 0.350″, with a total on-source integration time of 1693.440 s. The phase center was set at (RA, Dec) = (17:19:50.560, −37:00:09.370).

Standard ALMA calibration procedures were applied, including bandpass, phase, and amplitude calibration. Imaging was performed using the CASA 5.4.0-70 tclean task with Briggs weighting (robust = 0.5). Continuum emission was removed in the uv-plane using the uvcontsub task, after which spectral cubes were produced for all detected molecular transitions.

Spectral line identification and data analysis were performed using CASA, CARTA, and MADCUBA, and the final visualizations were produced with AstroPy [21–24].

Results and discussion

The 1.3 mm continuum emission toward G350.29+0.12 is presented in Figure 1. The continuum contours are drawn at 0.0017, 0.003056, 0.005348, 0.00764, 0.00988, 0.01216, 0.01444, 0.01672 Jy $beam^{-1}$. The synthesized beam, shown as the black ellipse in the lower-left corner, indicates the angular resolution of the map.

The continuum morphology reveals six compact peaks, indicated by "+" symbols. These peaks are grouped into two primary continuum sources: a bright northern core (G350.29+0.12 A) and a comparatively weaker southern core (G350.29+0.12 B). Both cores contain multiple substructures, although the northern core exhibits a more extended morphology. The projected separation between the two cores is approximately 0.51 pc, assuming a source distance of 11 kpc for G350.29+0.12 [25].

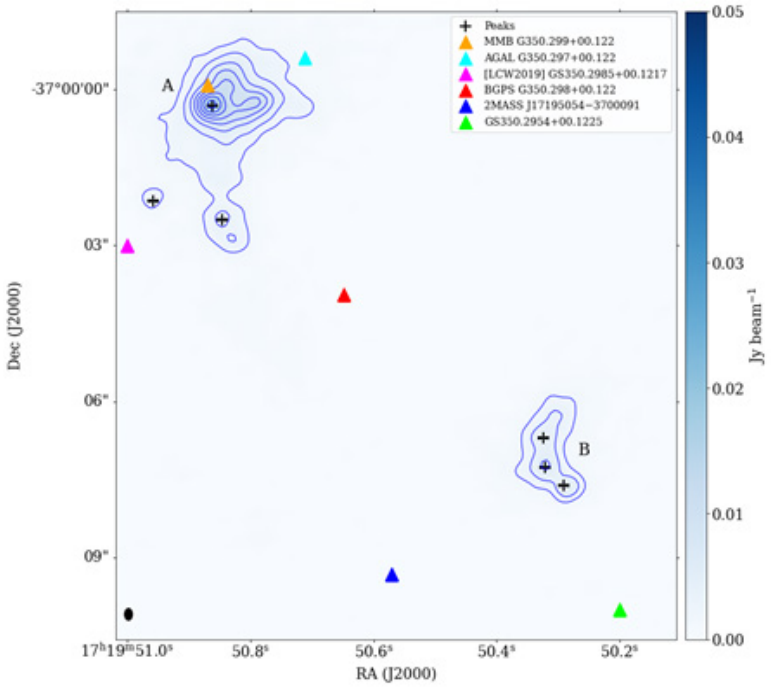

Figure 1 – Continuum map toward G350.29+0.12 at 1.3 mm

From a two-dimensional Gaussian fit to the continuum emission performed in CARTA, we derive the following parameters for the six identified peaks: right ascension (RA; J2000), declination (DEC; J2000), deconvolved source size, peak intensity I_{peak} (Jy beam^{-1}) and integrated flux density S (Jy). These fitted parameters are summarized in Table 1.

Table 1 – Observed parameters of the six 1.3 mm dust continuum peaks

№	RA (J2000) hh:mm:ss	DEC (J200) ° ′ ″	Source size (″)	I_{peak} (Jy/beam)	S (Jy)
1	17:19:50.562	–37:00:00.315	0.58 x 0.66	0.021 ± 0.004	0.042 ± 0.012
2	17:19:50.839	–37:00:02.683	0.84 x 0.24	0.004 ± 0.001	0.015 ± 0.005
3	17:19:50.958	–37:00:02.139	0.60 x 0.16	0.003 ±0.001	0.005 ± 0.002
4	17:19:50.321	–37:00:07.262	0.75 x 0.18	0.007 ± 0.002	0.019 ± 0.006
5	17:19:50.324	–37:00:06.702	0.80 x 0.23	0.006 ± 0.002	0.017 ± 0.006
6	17:19:50.291	–37:00:07.614	0.59 x 0.14	0.006 ±0.001	0.012 ± 0.004

In addition to the continuum peaks, several known sources are located near the molecular core. The methanol maser MMB G350.299+00.122 lies only ≈0.43″ from the main continuum peak in core A, indicating that this core is actively forming high-mass stars. Similarly, the nearby submillimeter source AGAL G350.297+00.122, located ≈2.03″ to the northwest, traces dense, cold gas surrounding the core. The positions of these sources support the interpretation that core A represents a site of ongoing massive star formation.

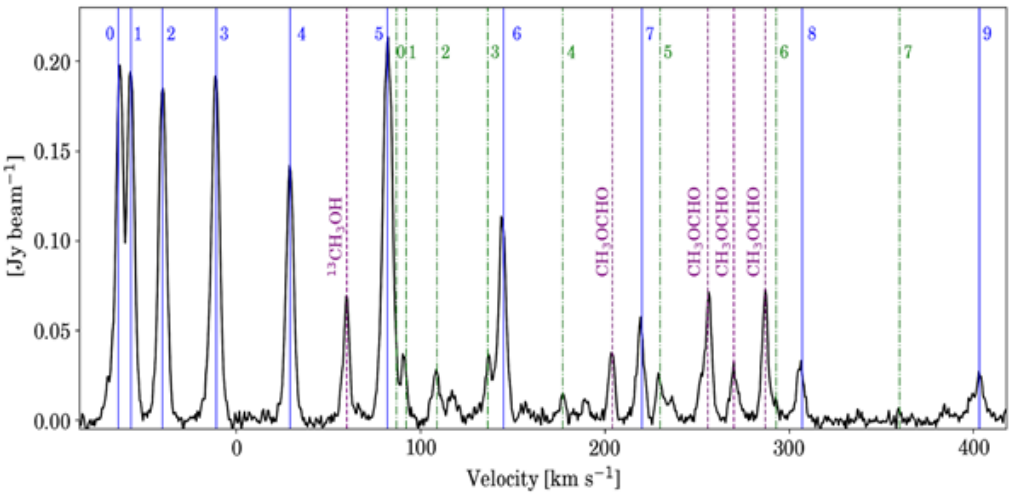

Figure 2 – Observed spectral profile toward the source G350.29+0.12.
The ordinate axis displays the flux density in Jy beam^{-1},
and the abscissa axis shows the radial velocity in km s^{-1}

We detected ten components (K = 0–9) of the CH_3CN J=14→13 rotational transition, indicated in blue in Figure 2. In addition, eight components (K = 0–7) of the $CH_3{}^{13}CN$ J=14→13 transition were identified, shown with green lines. Additional molecular transitions detected in this spectral window are highlighted with purple dashed lines. These lines, along with other prominent lines in the remaining windows, are summarized with their spectral parameters in Table 2.

Table 2 – Properties of spectral lines used in kinematic analysis

№	Line	Frequency (GHz)	Transition	E_{up} (K)	Core A	Core B
1	CS	244.935	5–4	35.26	Y	Y
2	SiO	256.518	6–5	43.76	N	Y
3	H_2CS	244.048	$7_{1,6}$–$6_{1,5}$	41.72	Y	N
4	CH_3OH	243.915	$5_{1,4}$–$4_{1,3}$ --	34.516	Y	Y
		256.228	$17_{3,15}$–$17_{2,16}$	404.79	Y	N
5	$^{13}CH_3OH$	256.351	$13_{3,11}$–$13_{2,12}$	256.14	Y	N
		257.422	$15_{(3,13)}$–$15_{(2,14)}$+-	321.79	Y	N
6	CH_3OCHO	257.252	$20_{(5,15)}$–$19_{(5,14)}$A	142.78	Y	N
		257.226	$20_{(5,15)}$–$19_{(5,14)}$E	142.78	Y	N
		257.241	$23_{(2,22)}$–$22_{(2,21)}$E	342.23	Y	N
		257.298	$21_{(9,12)}$–$20_{(9,11)}$A	377.18	Y	N
7	CH_3CN	257.527	14_0→13_0	92.70	Y	N
		257.522	14_1→13_1	99.85	Y	N
		257.508	14_2→13_2	121.28	Y	N
		257.483	14_3→13_3	156.99	Y	N
		257.448	14_4→13_4	206.98	Y	N
		257.404	14_5→13_5	271.23	Y	N
		257.349	14_6→13_6	349.72	Y	N
		257.285	14_7→13_7	442.45	Y	N
		257.211	14_8→13_8	549.38	Y	N
		257.127	14_9→13_9	670.50	Y	N
8	$CH_3{}^{13}CN$	257.400	14_0→13_0	92.65	Y	N
		257.395	14_1→13_1	99.80	Y	N
		257.380	14_2→13_2	121.23	Y	N
		257.355	14_3→13_3	156.94	Y	N
		257.321	14_4→13_4	206.93	Y	N
		257.276	14_5→13_5	271.17	Y	N
		257.222	14_6→13_6	349.67	Y	N
		257.158	14_7→13_7	442.33	Y	N

To evaluate the kinematics of the molecular gas, we generated the moment maps of the CH_3CN J=14→13. Figure 3 shows the moment maps of the K = 2 (first panel), K = 3 (second panel), K = 4 (third panel), and K = 6 (fourth panel) components. For each K-component, the moment 0 (integrated intensity map; top row), moment 1 (intensity-weighted velocity map; middle row) and moment 2 (velocity dispersion map; bottom row) are displayed.

The moment 0 maps show that the molecular gas is detected only toward core G350.29+0.12 A. The integrated intensities of CH_3CN K = 2 and K = 3 components reach a maximum of 1.25 Jy beam^{-1} km s^{-1}, whereas K = 4 and K = 6 exhibit lower peak intensities of 1 Jy beam^{-1} km s^{-1}, coinciding with the primary continuum peak. This spatial correspondence indicates that the CH_3CN emission arises from the densest and warmest portion of the core traced by the dust [26].

The moment 1 maps reveal a well-defined velocity gradient across the core. Within the CH_3CN-emitting region, velocities range from approximately –64 km s^{-1} to –62 km s^{-1}, corresponding to an amplitude of ~2 km s^{-1}. The gradient is oriented from northwest to southeast and is consistent with rotational motion. A similar velocity gradient has been reported for a comparable source in [27]. The moment 2 maps show clear differences in velocity dispersion among the CH_3CN K-components: the K = 2 and K = 4 components exhibit dispersions of approximately ~3 km^2 s^{-2}, while the K = 3 and K = 6 components display lower values of ~2.3 km^2 s^{-2}.

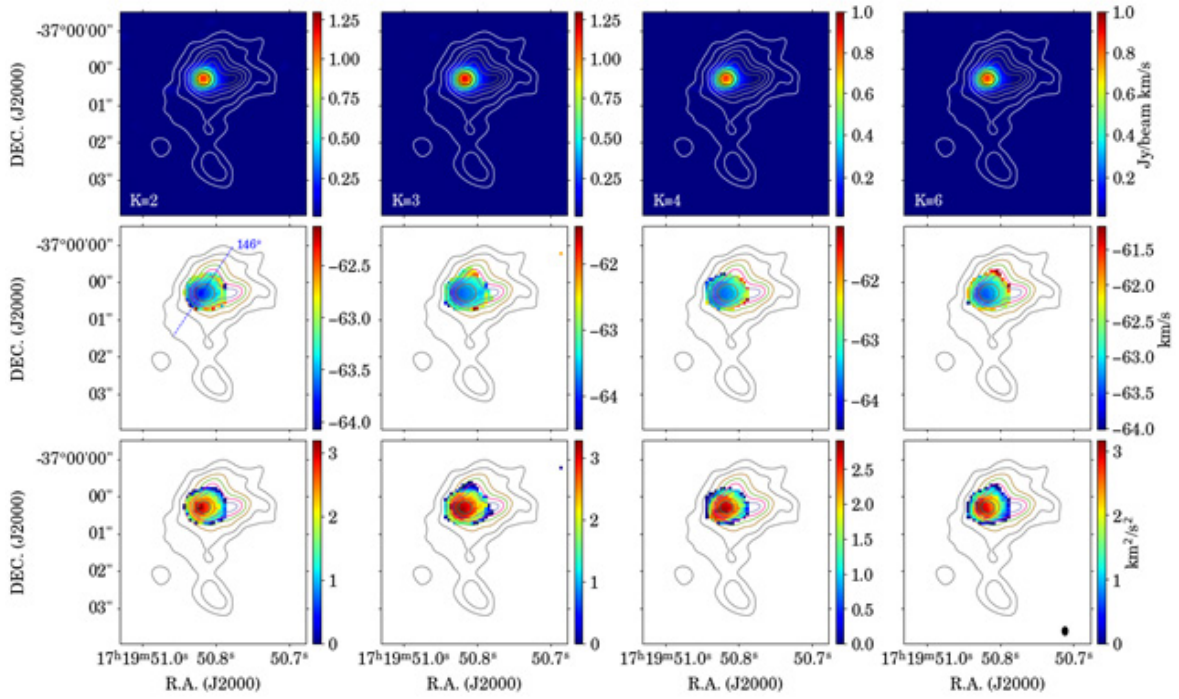

Figure 3 – Images of the velocity-integrated intensity (moment 0; top row), intensity-weighted velocity fields (moment 1; middle row), and velocity-dispersion maps (moment 2; bottom row) for the CH_3CN J = 14 → 13 transition, showing the K = 2, 3, 4 and 6 components

Figure 4 shows the position–velocity (PV) diagrams of the CH_3CN J = 12–11, K = 2, 3, 4 and 6 transitions, extracted along a position angle of 146°, corresponding to the direction of the moment-1 velocity gradient from northwest to southeast.

All diagrams reveal a compact velocity structure with a central peak, characteristic of a rotating hot molecular core. Each K-component exhibits a bright emission peak near zero offset, indicating that the bulk of the CH_3CN emission arises from the innermost ~1″ region.

The emission spans a velocity range of roughly −58 km s^{-1} to −68 km s^{-1} and shows a modest but systematic gradient along the PV axis. The overall symmetry about the central peak – with redshifted velocities on one side and blueshifted on the opposite – supports the presence of ordered rotational motions within the core.

The K = 4 and K = 6 transitions, tracing warmer and denser gas, are slightly more spatially compact but exhibit similar velocity gradients, whereas the K = 2 and K = 3 transitions extend over larger spatial and velocity ranges, consistent with their origin in less excited material.

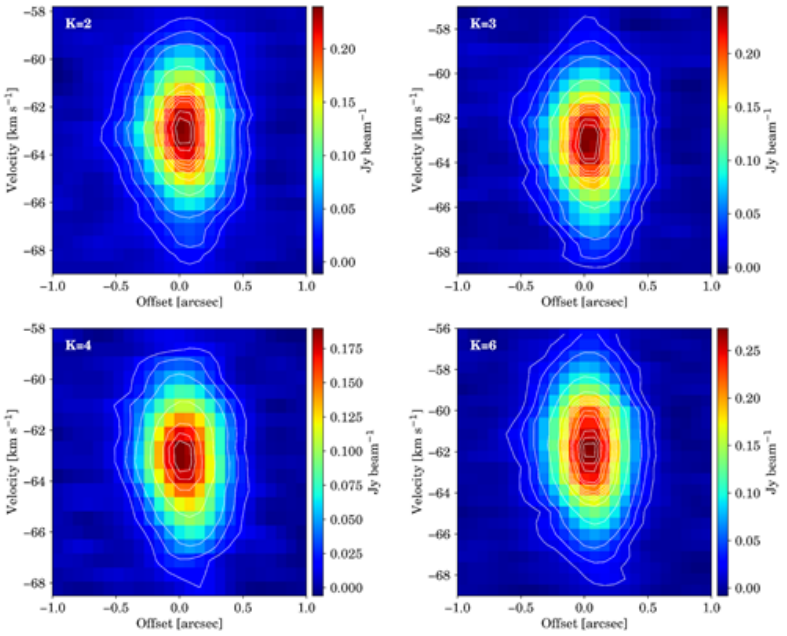

Figure 4 – Position–velocity (PV) diagrams of the CH_3CN

The rotational temperature of the molecular core was estimated using the CH_3CN and $CH_3{}^{13}CN$ transitions. The rotational population diagram was computed at the coordinates RA = 17:19:50.88, Dec = −37:00:00.407 (J2000). Rotational population diagrams were constructed with MAdrid Data CUBe Analysis (MADCUBA), providing a quantitative determination of both the rotational temperature and the column density.

Figure 4 shows the rotational population diagrams for CH_3CN and $CH_3{}^{13}CN$, where the logarithm of the level population divided by the statistical weight, $\ln(N_{up}/g_{up})$, is plotted against the upper-level energy E_{up}/k.

For CH_3CN, the best-fit slope corresponds to a rotational temperature of $T_{rot} = 360.6 \pm 34.8$ K, with a column density of $N = 4.4 \times 10^{13}$ cm^{-2} $\pm$ 1×10^{13}. This relatively high temperature suggests that CH_3CN traces warm and dense gas components typically associated with hot cores in massive star-forming regions.

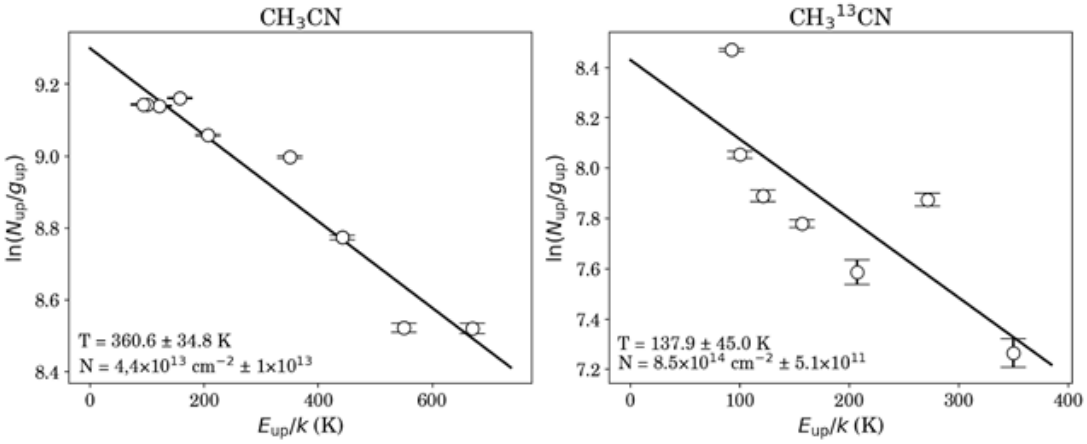

Figure 5 – Rotational population diagrams for the CH_3CN (left) and $CH_3{}^{13}CN$ (right) molecules. The vertical axis shows the logarithm of the level population divided by the statistical weight, $\ln(N_{up}/g_{up})$, and the horizontal axis shows the upper-level energy (E_{up}/k)

In contrast, the $CH_3{}^{13}CN$ isotopologue yields a lower rotational temperature of T_{rot} = 138 ± 45 K and a column density of N = 8.5 × 10^{14} cm^{-2} ± 5.1 × 10^{11}, consistent with emission arising from cooler and less abundant material. The difference in derived temperatures between the main and the ^{13}C isotopologue implies that CH_3CN predominantly probes the hotter, inner regions of the source, while $CH_3{}^{13}CN$ traces a comparatively cooler and more extended gas component [28].

Conclusion

We present ALMA 1.3 mm continuum and molecular line observations toward the high-mass star-forming region G350.29+0.12. The continuum map reveals two cores: a bright northern core G350.29+0.12 A and a weaker southern core G350.29+0.12 B. Core A exhibits six compact peaks embedded within a more extended structure.

We detect ten K-components of CH_3CN and eight K-components of $CH_3{}^{13}CN$. The integrated intensity maps show that CH_3CN emission is concentrated only at the peak of core A.

The intensity-weighted velocity map maps show a velocity gradient of about 2 km s^{-1} from northwest to southeast across the core. The PV diagrams of CH_3CN J = 12–11, extracted along a position angle of 146°, show a compact central peak and a clear velocity gradient, consistent with a rotating hot molecular core.

Rotational diagram analysis gives Trot = 360.6 ± 34.8 K for CH_3CN, tracing the hottest and densest gas, and Trot = 138 ± 45 K for $CH_3{}^{13}CN$, tracing cooler, more extended material.

These results indicate that G350.29+0.12 A is a rotating hot molecular core. Its association with the methanol maser MMB G350.299+00.122 and the submillimeter source AGAL G350.297+00.122 confirms that it is an active high-mass star-forming region.

Information on funding. This research has been funded by the Science Committee of the Ministry of Science and Higher Education of the Republic of Kazakhstan (grant no. AP26102915).

REFERENCES

1 Tan, J.C., Beltrán, M.T., Caselli, P., Fontani, F., Krumholz, M.R., McKee, C.F., and Stolte, A. Massive star formation. arXiv e-prints, arXiv:1402.0919 (2014). https://doi.org/10.48550/arXiv.1402.0919

2 Berdikhan, D., Esimbek, J., Henkel, C., Zhou, J., Tang, X., Liu, T., Wu, G., et al. Ammonia observations of Planck cold cores. Astronomy & Astrophysics, 684, A144 (2024). https://doi.org/10.1051/0004-6361/202348381

3 Komesh, T., Garay, G., Henkel, C., Omar, A., Estalella, R., Assembay, Z., et al. Infall motions in the hot core associated with the hypercompact H II region G345.0061+01.794 B. The Astrophysical Journal, 967(1), 15 (2024). https://doi.org/10.3847/1538-4357/ad3e7b

4 Tursun, K., Esimbek, J., Henkel, C., Tang, X., Wu, G., Li, D., et al. Ammonia observations towards the Aquila Rift cloud complex. Astronomy & Astrophysics, 643, A178 (2020). https://doi.org/10.1051/0004-6361/202037659

5 Berdikhan, D., Esimbek, J., Henkel, C., Xu, Y., Zhou, J., Liu, D., et al. Cloud–cloud collision and star formation in G013.313+0.193. Astronomy & Astrophysics, 699, A137 (2025). https://doi.org/10.1051/0004-6361/202453285

6 Fukui, Y., Habe, A., Inoue, T., Enokiya, R., and Tachihara, K. Cloud–cloud collisions and triggered star formation. Publications of the Astronomical Society of Japan, 73(Suppl. 1), S1–S34 (2021). https://doi.org/10.1093/pasj/psaa103

7 Sun, M., Esimbek, J., Henkel, C., Zhou, J., Wu, G., He, Y., Li, D., Tang, X., Komesh, T., Berdikhan, D., Ma, Y., et al. Possible collision-induced outflows and triggered star formation in the molecular complex G34. Monthly Notices of the Royal Astronomical Society, (2026), staf2285. https://doi.org/10.1093/mnras/staf2285

8 Li, D., Henkel, C., Kraus, A., Tang, X., Baan, W., Esimbek, J., Wang, K., Wu, G., Liu, T., and Sobolev, A.M. Evidence for core–core collision in Barnard 68. The Astrophysical Journal, 985 (2), 230 (2025). https://doi.org/10.3847/1538-4357/add326

9 He, Y.X., Liu, H.L., Tang, X.D., Qin, S.L., Zhou, J.J., Esimbek, J., Pan, S.R., Li, D.L., Zhao, M.K., and Ji, W.G. Investigating the globally collapsing hub–filament cloud G326.611+0.811. The Astrophysical Journal, 957 (2), 61 (2023). https://doi.org/10.3847/1538-4357/acf766

10 Zhang, W.J., Zhou, J.J., Esimbek, J., Baan, W., He, Y.X., Tang, X.D., Li, D.L., Ji, W.G., Wu, G., Ma, Y., Li, J., Zhou, D.D., Tursun, K., and Komesh, T. Kinematics and star formation of hub-filament systems in W49A. Astronomy & Astrophysics, 688, A99 (2024). https://doi.org/10.1051/0004-6361/202348580

11 Treviño-Morales, S.P., Fuente, A., Sánchez-Monge, Á., et al. Dynamics of cluster-forming hub-filament systems: the case of the high-mass star-forming complex Monoceros R2. Astronomy & Astrophysics, 629, A81 (2019). https://doi.org/10.1051/0004-6361/201935260

12 Ma, Y., Zhou, J.J., Esimbek, J., Baan, W., Li, D.L., Tang, X.D., He, Y.X., Ji, W.G., Zhou, D.D., Wu, G., Tursun, K., and Komesh, T. Gravitational collapse and accretion flows in the hub filament system G323.46–0.08. Astronomy & Astrophysics, 676, A15 (2023). https://doi.org/10.1051/0004-6361/202346248

13 Shen, H., Esimbek, J., Henkel, C., Li, D.L., Zhou, J.J., He, Y.X., Tang, X.D., Wu, G., Komesh, T., Tursun, K., Zhou, D.D., Ma, Y., Sailanbek, S., and Berdikhan, D. Triggered and dispersed under feedback of super H II region W4. Astronomy & Astrophysics, 693, A21 (2025). https://doi.org/10.1051/0004-6361/202450914

14 Komesh, T., Esimbek, J., Baan, W., Zhou, J., Li, D., Wu, G., He, Y., Sailanbek, S., Tang, X., and Manapbayeva, A. H_2CO and H110α observations toward the Aquila Molecular Cloud. The Astrophysical Journal, 874 (2), 172 (2019). https://doi.org/10.3847/1538-4357/ab0ae3

15 Imanaly, E., Esimbek, J., Baan, W., Wu, G., Zhou, J., Li, D., et al. Formaldehyde in the Cygnus-X region. Monthly Notices of the Royal Astronomical Society, 542(3), 2074–2086 (2025). https://doi.org/10.1093/mnras/staf1346

16 Imanaly, E., Esimbek, J., Baan, W., Wu, G., Zhou, J., Li, D., Tang, X., He, Y., Komesh, T., Zhou, D., Tursun, K., Ma, Y., Berdikhan, D., Sobolev, A.M., and Jandaolet, Q. Formaldehyde in the Cygnus-X region. Monthly Notices of the Royal Astronomical Society, 542 (3), 2074–2086 (2025). https://doi.org/10.1093/mnras/staf1346

17 He, Y.X., Henkel, C., Zhou, J.J., Esimbek, J., Stutz, A.M., Liu, H.L., Ji, W.G., Li, D.L., Wu, G., Tang, X.D., Komesh, T., and Sailanbek, S. Extended HNCO, SiO, and HC_3N emission in 43 southern star-forming regions. The Astrophysical Journal Supplement Series, 253 (1), 2 (2021). https://doi.org/10.3847/1538-4365/abd0fb

18 Komesh, T., Baan, W., Esimbek, J., Zhou, J., Li, D., Wu, G., He, Y., Rosli, Z., and Ibraimov, M. Studies of the distinct regions due to CO selective dissociation in the Aquila molecular cloud. Astronomy & Astrophysics, 644, A46 (2020). https://doi.org/10.1051/0004-6361/202038632

19 Abdullayev, Z., Komesh, T., Grossan, B., Abdikamalov, E., Maksut, Z., Krugov, M., Myrzakul, S., et al. Early-time optical spectral shape measurements of GRB 200925B. Revista Mexicana de Astronomía y Astrofísica (Serie de Conferencias), 59, 109–113 (2025). https://doi.org/10.22201/ia.14052059p.2025.59.20

20 Kalenskii, S.V., Promislov, V.G., Alakoz, A., Winnberg, A.V., and Johansson, L.E. Probing the properties of methyl cyanide sources. Astronomy & Astrophysics, 354, 1036–1040 (2000). https://adsabs.harvard.edu/full/2000A%26A...354.1036K

21 The CASA Team, Bean, B., Bhatnagar, S., et al. CASA: The Common Astronomy Software Applications for Radio Astronomy. Publications of the Astronomical Society of the Pacific, 134, 114501 (2022). https://doi.org/10.1088/1538-3873/ac9642

22 Comrie, A., Wang, K.-S., Hsu, S.-C., Moraghan, A., Harris, P., Pang, Q., Pińska, A., Chiang, C.-C., Simmonds, R., Chang, T.-H., Jan, H., and Lin, M.-Y. CARTA: The Cube Analysis and Rendering Tool for Astronomy. Publications of the Astronomical Society of the Pacific, 133, 104505 (2021). https://ui.adsabs.harvard.edu/abs/2021ascl.soft03031C

23 Martín, S., Martín-Pintado, J., Blanco-Sánchez, C., Rivilla, V.M., Rodríguez-Franco, A., and Rico-Villas, F. Spectral line identification and modelling (SLIM) in the MAdrid Data CUBe analysis (MADCUBA) package: Interactive software for data cube analysis. Astronomy & Astrophysics, 631, A159 (2019). https://doi.org/10.1051/0004-6361/201936144

24 Astropy Collaboration, Robitaille, T.P., Tollerud, E.J., et al. Astropy: A community Python package for astronomy. Astronomy & Astrophysics, 558, A33 (2013). https://doi.org/10.1051/0004-6361/201322068

25 Xu, Y., Voronkov, M.A., Pandian, J.D., Li, J.J., Sobolev, A.M., Brunthaler, A., Ritter, B., and Menten, K.M. Absolute positions of 6.7-GHz methanol masers. Astronomy & Astrophysics, 507 (2), 1117–1139 (2009). https://doi.org/10.1051/0004-6361/200912135

26 Remijan, A., Sutton, E.C., Snyder, L.E., Friedel, D.N., Liu, S.-Y., and Pei, C.-C. High-resolution observations of methyl cyanide (CH_3CN) toward the hot core regions W51e1/e2. The Astrophysical Journal, 606 (2), 917–926 (2004). https://doi.org/10.1086/383120

27 Omar, A., Abdirakhman, A., Alimgazinova, N., Kyzgarina, M., Naurzbayeva, A., Islyam, Z., Turekhanova, K., Demessinova, A., and Manapbayeva, A. ALMA Observations of G333.6–0.2: Molecular and Ionized Gas Environment. Galaxies, 13 (4), 73 (2025). https://doi.org/10.3390/galaxies13040073

28 Andron, I., Gratier, P., Majumdar, L., Vidal, T.H.G., Coutens, A., Loison, J.-C., and Wakelam, V. Methyl cyanide (CH_3CN) and propyne (CH_3CCH) in the low-mass protostar IRAS 16293–2422. Monthly Notices of the Royal Astronomical Society, 481 (4), 5651–5659 (2018). https://doi.org/10.1093/mnras/sty2680

[1]Абдирахман А.,
магистрант, ORCID ID: 0009-0002-0532-964,
e-mail: armiyaqyzyaidana@gmail.com
[1,2*]Омар А.,
PhD ORCID ID: 0000-0002-5604-3742,
*e-mail: omaruzhan@gmail.com
[1]Ислям Ж.,
магистрант, ORCID ID: 0009-0006-5496-4501,
e-mail:islyamovzhomart@gmail.com
[1,2]Әлімғазинова Н., .,
ф.-м.ғ.к., ORCID ID: 0000-0002-4596-1855,
e-mail: Nazgul.Alimgazinova@kaznu.kz
[1,2]Демессинова А А.,
PhD, ORCID ID: 0000-0001-5049-9338,
e-mail: aizat.dem@gmail.com
[1] Нодяров А.,
PhD, ORCID ID: 0000-0002-0045-5457,
e-mail: nodyarov.atilkhan@gmail.com
[3]Туяқбаева D.,
магистрант, ORCID ID: 0009-0003-8572-1850,
e-mail: duria1510@outlook.com
[2,4]Манапбаева А.,
PhD, ORCID ID: 0000-0002-0322-1509,
e-mail: manapbayeva.arailym@gmail.com
[1] Әділжан К.
докторант, ORCID ID: 0000-0003-4136-3935,
e-mail: kami_adilzhan@mail.ru
[5]Шаймолдин N.,
докторант, ORCID ID: 0000-0001-9557-8590,
e-mail: nurzhan@xao.ac.cn

[1]Әл-Фараби атындағы Қазақ ұлттық университеті, Алматы қ., Қазақстан
[2]Әл-Фараби атындағы Қазақ ұлттық университетінің Эксперименттік және теориялық физика институты, Алматы қ., Қазақстан
[3]Ш. Уәлиханов атындағы Көкшетау университеті, Көкшетау қ., Қазақстан
[4]Қазақ ұлттық қыздар педагогикалық университеті, Алматы қ., Қазақстан
[5]Қытай Ғылым академиясының Шыңжаң астрономиялық обсерваториясы, Үрімші қ., Қытай

G350.29+0.12 МАССИВТІ ЖҰЛДЫЗ ТҮЗУШІ АЙМАҒЫНЫҢ КИНЕМАТИКАСЫ МЕН ҚҰРЫЛЫМЫ

Аңдатпа

Біз G350.29+0.12 массивті жұлдыз түзілу аймағына бағытталған жоғары бұрыштық ажыратымдылықтағы 1,3 мм континуумдық және молекулалық сызықтық бақылауларды ұсынамыз. Бақылаулар CH_3CN

және $CH_3{}^{13}CN$ молекулаларының айналмалы ауысулары арқылы жүргізілді. Континуумдық сәуле шығару екі негізгі ядроны айқындайды: жарық әрі ықшам солтүстік ядро G350.29+0.12 A және әлсіздеу оңтүстік ядро G350.29+0.12 B. A ядросы кеңейтілген сәуле шығару аясында орналасқан алты ықшам ішкі құрылымды көрсетеді. CH_3CN J = 14→13 және $CH_3{}^{13}CN$ J = 14→13 ауысуларының бірнеше K-компоненттері анықталды, олардың сәуле шығару көздері негізінен A ядросымен байланысты. CH_3CN үшін момент 0 карталары интегралдық интенсивтіліктің негізгі континуум позициясында максимумға жететінін көрсетеді, бұл молекулалық сәуле шығарудың жылы әрі тығыз газды сипаттайтынын білдіреді. Момент 1 карталары A ядросы бойымен солтүстік-батыстан оңтүстік-шығысқа бағытталған шамамен ∼2 км/с жылдамдық градиентін анықтайды, ал момент 2 карталары K-компоненттерге тәуелді жылдамдық дисперсиясының өзгерістерін көрсетеді. PV диаграммалары айналмалы қозғалыстың бар екенін дәлелдейді: олар орталық максимуммен және жүйелі градиенттермен сипатталатын ықшам жылдамдық құрылымы түрінде көрінеді. Айналмалы температураны талдау CH_3CN үшін $T_{(rot)} = 360,6 \pm 34,8$ K мәнін береді, бұл ең ыстық әрі тығыз газды сипаттайды, ал $CH_3{}^{13}CN$ үшін $T_{(rot)} = 138 \pm 45$ K алынған, ол салыстырмалы түрде салқынырақ әрі кеңейтілген затқа тән. Жалпы алғанда, бұл нәтижелер G350.29+0.12 A нысаны белсенді массивті жұлдыз түзілу процесінен өтіп жатқан айналмалы ыстық молекулалық ядро екенін көрсетеді.

Тірек сөздер: массивті жұлдыз түзілу аймағы; молекулалық сәулелену; PV талдауы; айналмалы температура; ыстық молекулалық ядро.

[1]Абдирахман А.,
магистрант, ORCID ID: 0009-0002-0532-964,
e-mail: armiyaqyzyaidana@gmail.com
[1,2] *Омар А.,
PhD, ORCID ID: 0000-0002-5604-3742,
*e-mail: omaruzhan@gmail.com
[1]Ислям Ж.,
магистрант, ORCID ID: 0009-0006-5496-4501,
e-mail: islyamovzhomart@gmail.com
[1,2]Алимгазинова Н.,
к.ф.-м.н., ORCID iD: 0000-0002-4596-1855,
e-mail: Nazgul.Alimgazinova@kaznu.kz
[1,2]Демессинова А А.,
PhD, ORCID iD: 0000-0001-5049-9338
e-mail:aizat.dem@gmail.com
[1]Нодяров А.,
PhD, ORCID iD: 0000-0002-0045-5457,
e-mail: nodyarov.atilkhan@gmail.com
[3]Туяқбаева D.,
магистрант, ORCID ID: 0009-0003-8572-1850,
e-mail: duria1510@outlook.com
[2,4]Манапбаева А.,
PhD, ORCID ID: 0000-0002-0322-1509,
e-mail: manapbayeva.arailym@gmail.com
[1]Адилжан К.,
докторант, ORCID ID: 0000-0003-4136-3935,
e-mail: kami_adilzhan@mail.ru
[5]Шаймолдин Н.,
докторант, ORCID ID: 0000-0001-9557-8590,
e-mail: nurzhan@xao.ac.cn

[1]Казахский национальный университет им. аль-Фараби, г. Алматы, Казахстан
[2]Институт экспериментальной и теоретической физики,

Казахский национальный университет им. аль-Фараби, г. Алматы, Казахстан
[3]Университет имени Ш. Уалиханова, г. Кокшетау, Казахстан
[4]Казахский национальный женский педагогический университет, г. Алматы, Казахстан
[5]Астрономическая обсерватория Синьцзянского отделения Китайской академии наук, г. Урумчи, Китай

АНАЛИЗ МОЛЕКУЛЯРНЫХ ЛИНИЙ В ОБЛАСТИ G23.21−0.38 ПО ДАННЫМ ALMA: СВИДЕТЕЛЬСТВА ВРАЩЕНИЯ И ГРАДИЕНТОВ ВОЗБУЖДЕНИЯ

Аннотация

Мы представляем наблюдения континуума на длине волны 1.3 мм с высоким угловым разрешением, а также молекулярных линий в области массивного звездообразования G350.29+0.12, выполненные с использованием вращательных переходов CH_3CN и $CH_3{}^{13}CN$. Континуумное излучение разрешает два основных ядра: яркое компактное северное ядро G350.29+0.12 A и более слабое южное ядро G350.29+0.12 B. Ядро A демонстрирует шесть компактных субструктур, вложенных в более протяженное излучение. Обнаружены множественные K-компоненты переходов CH_3CN J = 14→13 и $CH_3{}^{13}CN$ J = 14→13, при этом излучение преимущественно исходит из ядра A. Карты момента 0 для CH_3CN показывают, что интегральные интенсивности достигают максимума в положении основного континуумного источника, указывая на то, что молекулярное излучение трассирует теплый и плотный газ. Карты момента 1 выявляют выраженный градиент скорости порядка ∼2 км/с через ядро A, ориентированный с северо-запада на юго-восток, тогда как карты момента 2 демонстрируют зависящие от K-компоненты вариации дисперсии скоростей. Диаграммы положение–скорость дополнительно указывают на организованные вращательные движения, проявляющиеся в виде компактной скоростной структуры с центральным максимумом и систематическими градиентами. Анализ вращательной температуры дает $T_{(rot)} = 360.6 \pm 34.8$ K для CH_3CN, что указывает на наиболее горячий и плотный газ, и $T_{(rot)} = 138 \pm 45$ K для $CH_3{}^{13}CN$, что согласуется с более холодным и протяженным веществом. В совокупности эти результаты демонстрируют, что G350.29+0.12 A является вращающимся горячим молекулярным ядром, находящимся на стадии активного массивного звездообразования.

Ключевые слова: область массивного звездообразования, молекулярное излучение, анализ PV, вращательная температура, горячее молекулярное ядро.